# Design of a soft x-ray emission spectrograph for the study of biologically relevant molecules

O. Fuchs, L. Weinhardt, C. Heske, E. Umbach, University of Würzburg

R. Follath, Bessy II, Berlin

Y.D. Chuang, W.R. McKinney, Z. Hussain, Advanced Light Source

April 2003

# Contents

**1 Introduction and outline** **1**

**2 The optical design** **2**

**3 Design considerations and methods** **4**
3.1 The one-grating concept . . . . . 4
3.2 Throughput . . . . . 4
3.2.1 Optimizing the grazing incidence angle . . . . . 5
3.3 Resolving power . . . . . 5
3.3.1 The source-size limited resolution . . . . . 7
3.3.2 The pixel-size limited resolution . . . . . 7
3.3.3 Imaging aberrations . . . . . 8
3.3.4 Outer versus inner diffraction orders . . . . . 9
3.4 Optimizing the VLS-parameters . . . . . 11

**4 Performance** **13**
4.1 Energy resolution . . . . . 13
4.2 Throughput . . . . . 13
4.3 Ray tracing . . . . . 14

**5 Summary** **20**

# Chapter 1

# Introduction and outline

This work describes the optimized design of a soft x-ray emission spectrograph with moderate resolution and high throughput, dedicated to the study of biologically relevant molecules containing carbon, nitrogen, oxygen and sulfur atoms. The desired emission lines are sulfur $L_{2,3}$, carbon K, nitrogen K, and oxygen K, with approximate photon energies of 150, 280, 390, and 525 eV.

In chapter 2, the principle of the spectrograph is explained with the help of a schematic drawing, and the parameters of the final design are listed. In chapter 3 the basic design strategies which led to the final design are discussed. The methods used to obtain and check the optimum parameters, in particular the ruling parameters of the VLS-grating, are described in detail. Finally, the theoretical performance and ray traced images of the chosen design are shown and discussed in chapter 4.

# Chapter 2

# The optical design

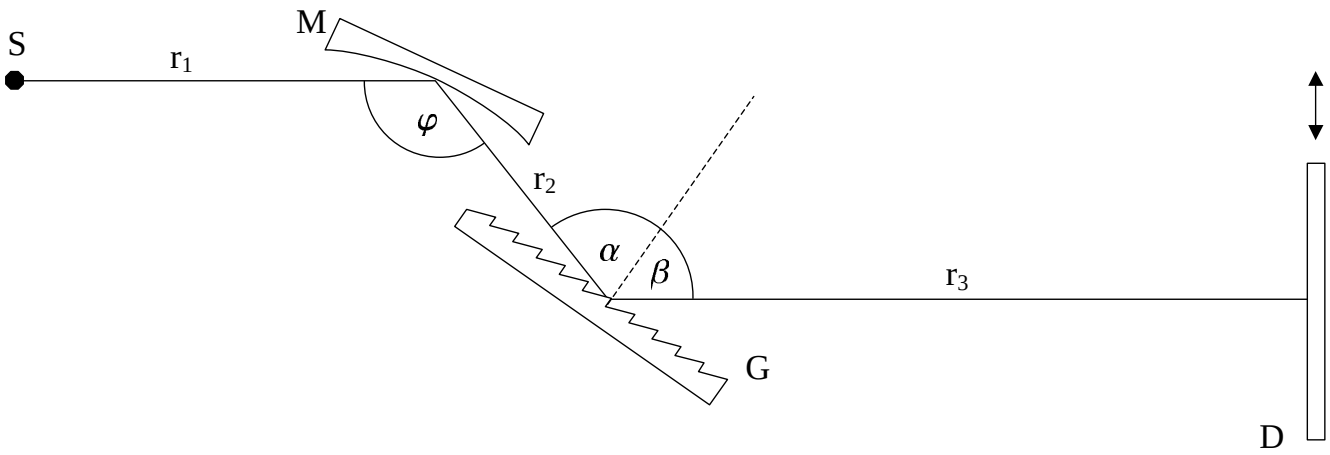


Figure 2.1: Optical layout of the spectrograph

The basic optical layout shown in Fig. 2.1 is derived from an existing spectrograph design described in [1, 2]. The refocused illuminated sample area itself serves as the source S, which is imaged by a spherical mirror M and a subsequent blazed planar varied-line-spaced grating (VLS-grating) G as energy dispersive component operating in inner (positive) orders ($\alpha > \beta$). The spectral rays emanating from the grating illuminate the detector D (an uncoated back-illuminated CCD-camera) at normal incidence, delivering an energy dispersed spectrum "in one shot" without the need of mechanical scanning. In order to tune the spectrometer to a desired central energy, the detector is shifted perpendicular to the incoming ray, i.e., parallel to the detector surface, while the incidence angle on the grating $\alpha$ remains fixed.

# List of design parameters

### Angles and distances

| | | |
|---|---|---|
| $\varphi$ | = | 172.000° |
| $\alpha$ | = | 87.886° |
| $\beta$ | = | 84.114° |

| | | |
|---|---|---|
| $r_1$ | = | 400.00 mm |
| $r_2$ | = | 100.05 mm |
| $r_3$ | = | 1,000.00 mm |

### Mirror specifications

| | |
|---|---|
| dimensions: | 20 x 80 mm |
| radius of curvature: | $R$=8,410 mm |

### Grating specifications

| | |
|---|---|
| dimensions: | 20 x 110 mm |
| blaze angle: | 1.79° for inner (positive) orders |
| central groove density: | $a_0 = 600$ lines/mm |
| VLS-parameters: | $a_1 = 1.19634$ lines/mm$^2$ |
| | $a_2 = 1.27512 \cdot 10^{-3}$ lines/mm$^3$ |
| | $a_3 = 1.11401 \cdot 10^{-6}$ lines/mm$^4$ |
| rule density [lines/mm]: | $n(w) = (600 + 1.19634\ w + 1.27512 \cdot 10^{-3}\ w^2 + 1.11401 \cdot 10^{-6}\ w^3)$ |
| | ($w$ in mm) |

### Detector specifications

| | |
|---|---|
| dimensions: | 27.6 x 27.6 mm |
| pixel dimensions: | 13.5 x 13.5 $\mu$m |

# Chapter 3

# Design considerations and methods

## 3.1 The one-grating concept

Since blazed VLS-gratings with complex line spacing variations have to be ruled mechanically and are therefore expensive, it is a good idea to cover the desired energy range of 130-540 eV with only one grating. This is achieved by using suitable diffraction orders which appear in a narrow angular range, yet without showing spectral overlap, giving the advantage of very similar resolving powers for all four emission lines, a very high blaze efficiency, and comparably small imaging aberrations. A suitable choice fulfilling these conditions is to detect the sulfur $L_{2,3}$ emission (150 eV) in the $1^{st}$ diffraction order, carbon K (280 eV) in $2^{nd}$, nitrogen K (390 eV) in $2^{nd}$, and oxygen K (525 eV) in $3^{rd}$ order. In the following these four cases will be referred to by using the symbols S, C, N, O. The frequently occurring photon energy of 162 eV in first diffraction order corresponds to the mean wavelength of these four cases and gives a good impression of the average performance of the instrument regarding the spot-size and pixel-size limited energy resolving power.

In order to reduce the development costs, the original mechanical design was maintained as far as it did not compromise the optical performance.

## 3.2 Throughput

The total throughput $\eta$ of the instrument can be defined as the ratio of the detected intensity to the total emitted intensity of the sample surface into half space:

$$\boxed{\eta = \frac{\Delta\varphi\Delta\psi}{2\pi \text{ sterad}} \cdot \mathcal{R}_{\text{mirror}} \cdot \mathcal{E}_{\text{grating}} \cdot \mathcal{Q}_{\text{detector}}} \tag{3.1}$$

where $\Delta\varphi$ is the acceptance angle in the non-dispersive (horizontal) direction, $\Delta\psi$ is the acceptance angle in the dispersive (vertical) direction, $\mathcal{R}_{\text{mirror}}$ is the reflectivity of the mirror, $\mathcal{E}_{\text{grating}}$ is the diffraction efficiency of the grating, and $\mathcal{Q}_{\text{detector}}$ is the quantum efficiency of the detector. The latter can only be influenced by the choice of detector and the incidence angle on the detector, which is 90° (normal incidence) in this design and therefore ideal.

### 3.2.1 Optimizing the grazing incidence angle

The reflectivities are determined by the coating material, its surface roughness, and the grazing incidence angle $\theta$. At photon energies below the Nickel $L_{2,3}$-edge (≈850 eV), Ni has the highest reflectivity, making it the coating material of choice in our case.

Optical elements typically have a surface microroughness of approx. 10 Å, which is also assumed throughout this work.

A simple but effective method to determine the optimum zero order grazing incidence angle $\theta$ on the mirror and the grating is to maximize the merit function $\mathcal{M}(\theta)$ defined as

$$\boxed{\mathcal{M}(\theta) = \theta \cdot \mathcal{R}_{\mathrm{Ni}}^2(\theta)} \tag{3.2}$$

The angle-dependent reflectivity $\mathcal{R}_{\mathrm{Ni}}(\theta)$ is squared because the photons undergo two reflections at the mirror and the grating before being detected, and multiplying by $\theta$ takes the variation in the accepted solid angle at a given mirror and grating length into account.

Figure 3.1 shows $\mathcal{M}(\theta)$ for the four interesting photon energies of 150, 280, 390, and 525 eV, revealing a maximum for 280 and 390 eV at $\theta \approx 4.0°$. The reflectivities were calculated for an assumed surface roughness of 10 Å and unpolarized light by the program "REFLEC" [3]. $\theta = 4.0°$ leads only to a 11% loss for 525 eV and a 2.5% loss for 150 eV while being optimal for 280 and 390 eV and hence constitutes a very good compromise. Choosing $\theta = 4.0°$ leads to a deviation angle of 8.0° at the mirror. For the grating, which is operating in a constant incidence angle mode, the deviation angle depends on the photon energy. The incidence angle was chosen to be 87.886°, leading to a deviation angle of 8.0° for the center photon energy of 162 eV. The resulting reflectivities and the total transmission of the instrument are discussed in section 4.2.

A more complex optimization procedure, which optimizes $\theta$ at the mirror and the grating independently, derives a slightly higher throughput by choosing a steeper incidence on the grating while maintaining the mirror angle at 4.0°. However, this would reduce the energy dispersion of the grating significantly, and hence this approach was not pursued further.

## 3.3 Resolving power

The design goal was a theoretical energy resolving power $\frac{E}{\Delta E}$ of 1,000. Apart from minor contributions (e.g., fluctuations of the sample spot position, mechanical vibrations, etc.), the energy resolution is limited by three main factors:

- Source size
- Pixel size of the detector
- Imaging aberrations

In order to meet the design goal, all three factors have to be studied and adjusted independently. Ideally, the instrument should give the user some liberty in choosing the limiting factor by selecting appropriate experimental parameters. The central equation describing the energy dispersive

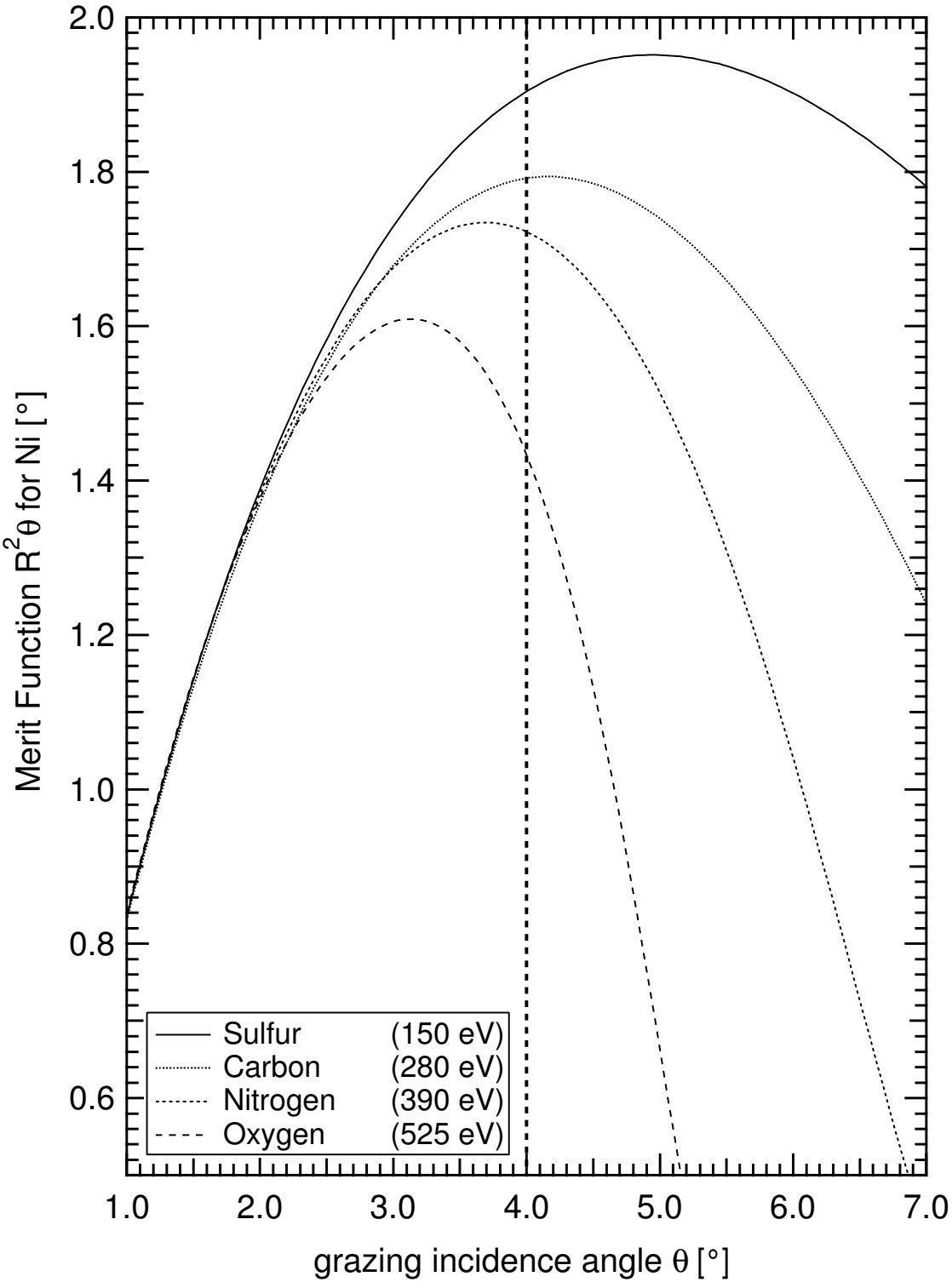


Figure 3.1: The merit function $\mathcal{M}(\theta) = R^2\theta$ for photon energies of 150, 280, 390, and 525 eV.

diffraction at the grating is the so-called grating equation [5]:

$$\boxed{\sin(\alpha) - \sin(\beta) = n \cdot m \cdot \frac{hc}{eE}} \tag{3.3}$$

$\alpha$ and $\beta$ are the grating incidence and exit angle, respectively, $n$ is the rule density, $m$ is the diffraction order, $h$ is Planck's constant, $c$ is the speed of light, $e$ is the elementary charge, and $E$ is the photon energy.

Solving 3.3 for $\beta$ and taking the derivative with respect to $E$ yields an expression for the angular dispersion $\frac{\mathrm{d}\beta}{\mathrm{d}E}$ of the grating:

$$\boxed{\frac{\mathrm{d}\beta}{\mathrm{d}E} = \frac{c \cdot h \cdot m \cdot n}{e \cdot E^2 \cdot \cos\beta}} \tag{3.4}$$

### 3.3.1 The source-size limited resolution

The source-size limited resolution is determined by the vertical size of the synchrotron spot $\Delta y$ on the sample, the total magnification $M = \frac{(r_2+r_3)\cdot\cos\alpha}{r_1\cdot\cos\beta}$ of the optics, and the energy dispersion $\frac{\mathrm{d}\beta}{\mathrm{d}E}\cdot r_3$ on the detector. In order to resolve two photon energies differing by $\Delta E_{\mathrm{source}}$, their images on the detector need to be separated by the size of the image of the source spot. This condition can be written as:

$$\boxed{\Delta y \cdot M = \frac{\mathrm{d}\beta}{\mathrm{d}E} \cdot \Delta E_{\mathrm{source}} \cdot r_3} \tag{3.5}$$

The source-size limited resolving power $\frac{E}{\Delta E}$ is then given by:

$$\boxed{\frac{E}{\Delta E_{\mathrm{source}}} = \frac{E \cdot \frac{\mathrm{d}\beta}{\mathrm{d}E} \cdot r_3}{\Delta y \cdot M} = \frac{E \cdot \frac{\mathrm{d}\beta}{\mathrm{d}E} \cdot r_3 \cdot r_1 \cdot \cos\beta}{\Delta y \cdot (r_2 + r_3) \cdot \cos\alpha}} \tag{3.6}$$

### 3.3.2 The pixel-size limited resolution

The second important quantity to consider is the spatial resolution of the detector, which is given by the pixel size. Since the narrowest possible peak in an energy spectrum should consist of at least 5 pixels, the pixel-size limited energy resolving power has to be about 3.5 times higher than the source-size limit (i.e. 3,500). This choice allows for an additional broadening of 1.5 pixels due to additional contributions such as imaging errors, fluctuations of the sample spot position, and mechanical vibrations.

In our case, with a given detector pixel size of 13.5 $\mu$m, the pixel-size limited energy resolving power is simply derived from equation 3.4 as:

$$\boxed{\frac{E}{\Delta E_{\mathrm{pixel}}} = \frac{E \cdot \frac{\mathrm{d}\beta}{\mathrm{d}E} \cdot r_3}{13.5\ \mu\mathrm{m}}} \tag{3.7}$$

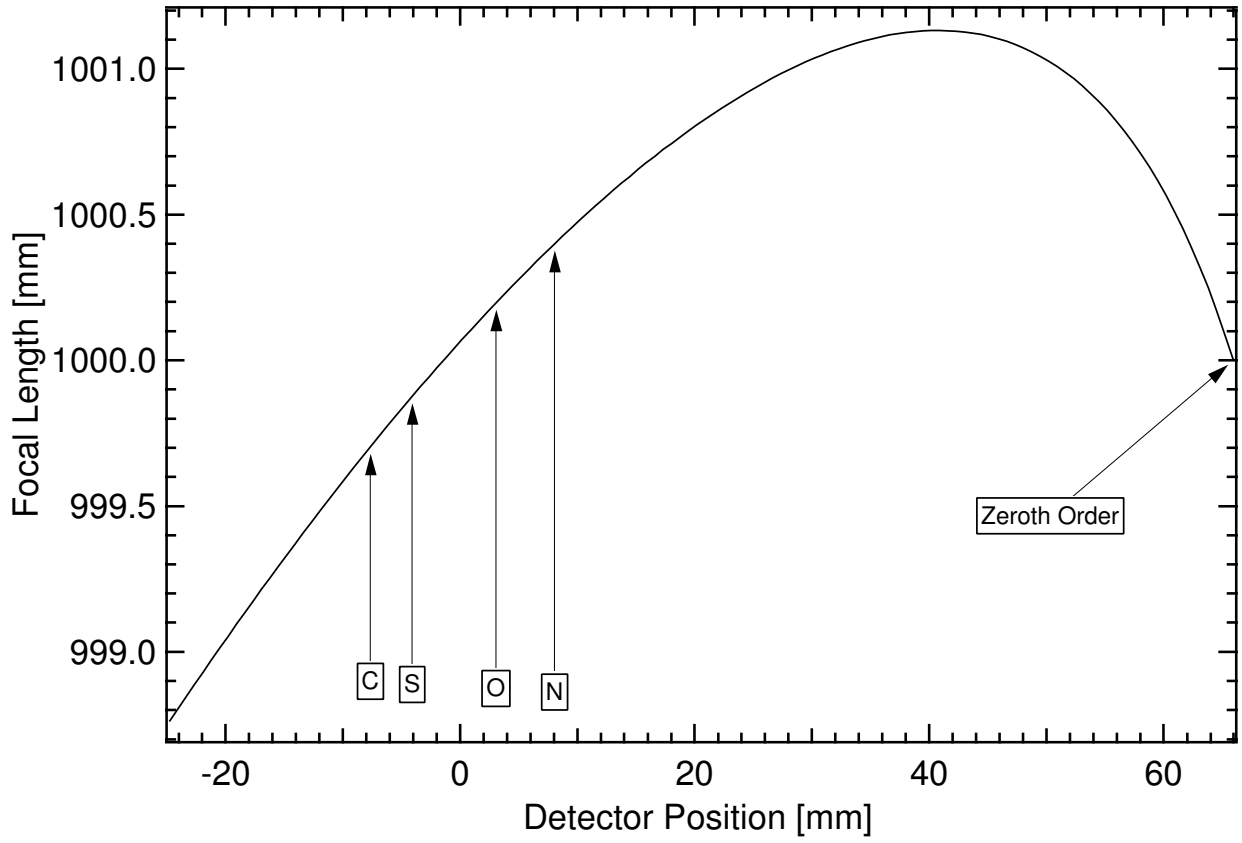


Figure 3.2: The focal length (measured from the grating position) as a function of the vertical position on the detector.

### 3.3.3 Imaging aberrations

**The defocus term**

Only the first order imaging aberration, the so-called defocus, can be easily studied analytically by considering the beam divergence at the detector and the deviation of the detector plane from the focus position. But because the VLS-parameters can be optimized to cancel the defocus term almost entirely, the variation of the focal length over the interesting wavelength range can be neglected.

Fig. 3.2 shows the focal length from the grating position as a function of the vertical position on the detector plane. The labels show where the four interesting energies of sulfur in first order (S), carbon in second order (C), nitrogen in second order (N), and oxygen in third order (O) appear on the detector. In this region the variation of the focal length is less than $\pm 0.5$ mm. Note that the VLS grating in zeroth order is acting like a plane mirror, i.e., the focal length in zeroth order is only determined by the radius of the mirror, which is chosen to give a focal length of 1 m for the grating. The slope of the focal length curve in Fig. 3.2 suggests that tilting the detector by 2.6°

(counterclockwise in Fig. 2.1) to align the detector tangential to the focal curve in the region of interest might improve the optical properties. However, a thorough analysis including the detector tilt as an additional degree of freedom in the process of minimizing the imaging aberrations shows that in fact the overall imaging aberrations get worse due to increasing higher order contributions. These contributions lead to a surprising result confirming the negligibility of the defocus term: the optimum detector tilt angle would be 0.5°, but in the clockwise direction (i.e., even further away from the focal curve)!

**The total imaging aberrations**

The overall imaging aberrations can not be expressed easily in analytical form. But since they are only important in the dispersive direction (in the non-dispersive direction the image is not focused), it is sufficient to consider only rays in the tangential (vertical) plane. The imaging aberrations of a given design can then be visualized by plotting the distance of the impinging point on the detector to its center versus the angular deviation from the central ray. Such plots give a variety of important information, e.g., the image broadening due to imaging aberrations as a function of vertical acceptance angle, which can be adjusted by reducing the mirror illumination with baffles. In Fig. 3.3 such a plot is shown for the photon energies of interest here as well as for the mean energy of 162 eV, for which the imaging errors are negligible. The parabolic shape identifies the main contributions as second-order terms (coma).

The fact that the imaging errors of the two most extreme wavelengths (carbon and nitrogen emission in $2^{\text{nd}}$ order) show opposite signs and are of comparable amplitude testifies the successful optimization of the VLS parameters, resulting in an optimum compromise for the relevant energies.

At all four photon energies, the imaging errors of the fully illuminated optics (i.e., 11.2 mrad vertical acceptance) are less than two detector pixels wide. They can be reduced arbitrarily by masking the mirror at the cost of intensity. For example, to reduce all imaging errors to less than a detector pixel (13.5 $\mu$m), one would have to reduce the vertical acceptance angle from 11.2 mrad to 8.5 mrad, as can be easily derived from Fig. 3.3.

### 3.3.4 Outer versus inner diffraction orders

Now we can use equations 3.6 and 3.7 to find an appropriate value for the central groove density $n$ of the grating. The search criterion was chosen to be a pixel-size limited resolving power of approx. 3500 at a photon energy of 162 eV and a deviation angle of 8° (see section 3.2.1). The groove density necessary to provide this resolution depends on the sign of the used diffraction order. Therefore we have to decide whether to use inner (positive) orders, where $\alpha$ is bigger than $\beta$ (i.e., the reflected ray is steeper than the incoming ray), or outer (negative) orders where $\alpha$ is smaller than $\beta$ (i.e., the incoming ray is steeper than the reflected ray). The pixel resolving power is determined by the angular dispersion, which is proportional to $n/\cos\beta$, as can be seen from equation 3.4. Since $\beta$ is closer to 90° in outer orders, the angular dispersion at a given rule density is significantly higher than in inner orders. The drawback of the outer orders is the much higher magnification of the grating $M_{\text{grating}} = \frac{\cos\alpha}{\cos\beta}$, which leads to a poor source-size limited resolving

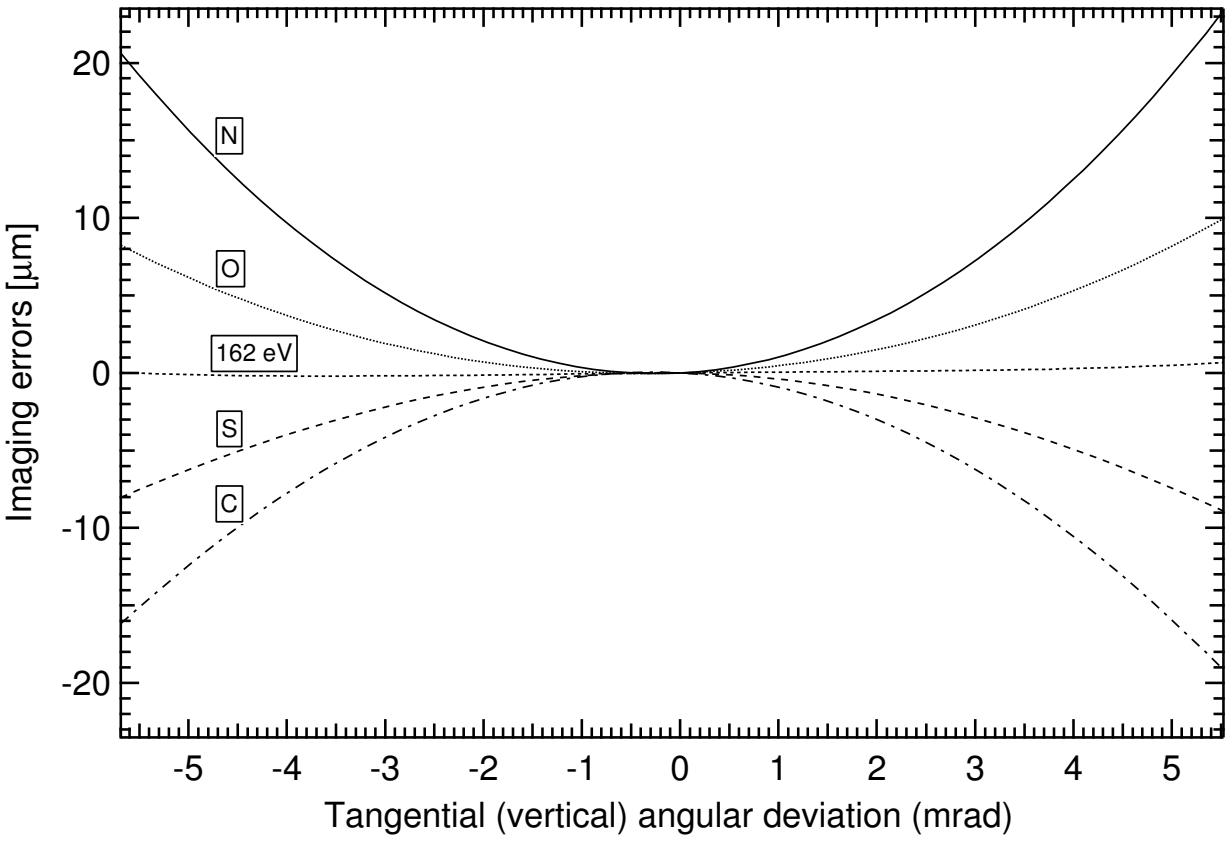


Figure 3.3: The imaging errors of the four relevant emission lines and the mean energy of 162 eV.

power if the source spot is larger than 10 $\mu$m. In inner orders the magnification is actually smaller than 1 and therefore the grating demagnifies, compensating part of the mirror magnification.

Groove densities leading to a pixel resolving power at 162 eV of approx. 3500 are 600 lines/mm in inner (positive) order, and 310 lines/mm in outer (negative) order. Both cases are shown in Fig. 3.4. Four arrows show the energies of the relevant emission lines. The pixel-size limited as well as the spot-size limited resolving powers of a 10 $\mu$m source are plotted. Note that for the inner orders the behavior of a constant incidence angle mount as in the final design is shown, whereas for outer orders, a constant deviation mount as in the design reported in [1, 2] was used. Both mounts are equivalent at $h\nu$=162 eV. The chosen line densities result in the design goal of a pixel-limited resolving power of approx. 3500 at 162 eV in both cases. However, large differences between inner and outer orders exist when computing the total magnification. In inner orders, the total magnification of 1 (grating magnification: 0.36) is very small compared to 4.5 (grating magnification: 1.64) in outer orders, leading to a much higher source-size limited resolving power for the inner orders. This allows for an illuminated sample spot as big as 10,000 x 30 $\mu$m$^2$ to meet the design goal of a minimum resolving power of 850. The resulting lower photon flux density on the sample is important for examining materials that are subject to beam damage. Furthermore,

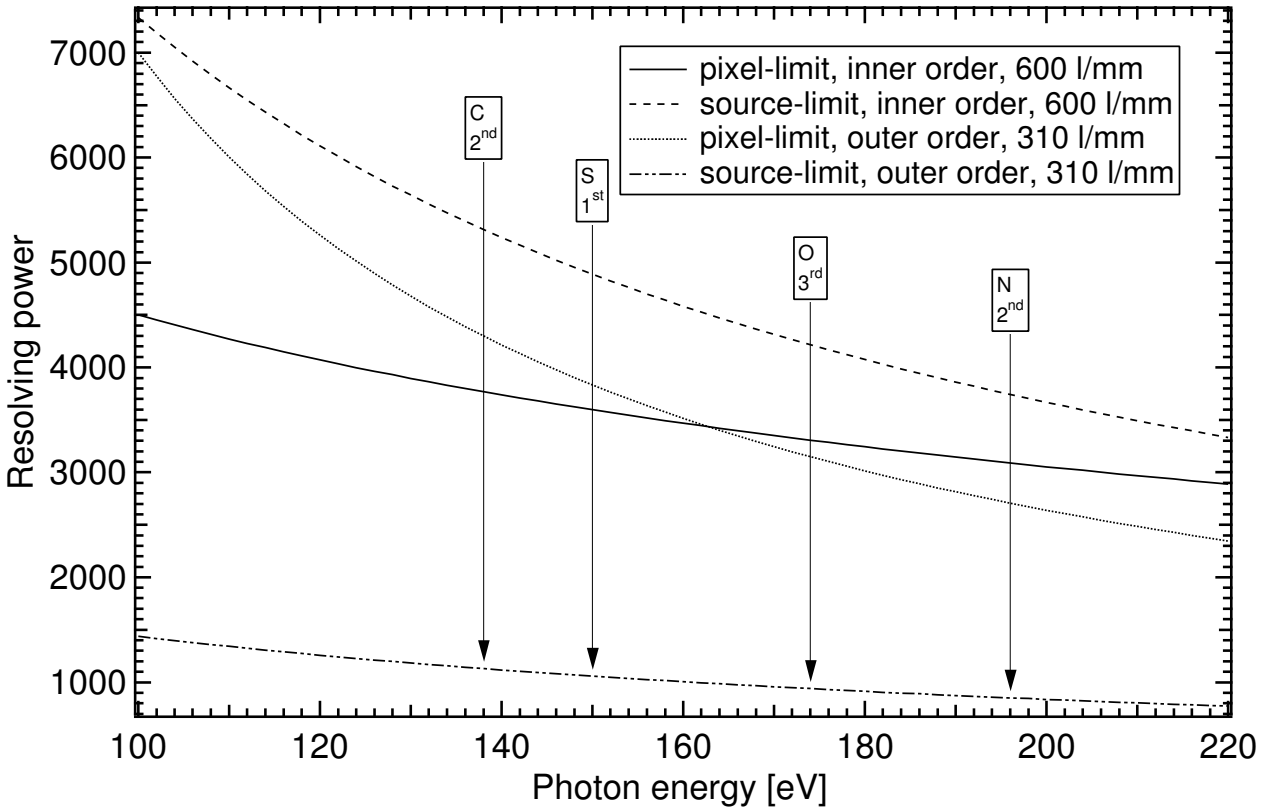


Figure 3.4: Resolving power of inner and outer orders. The source-limits are calculated for a 10 $\mu$m wide source. The relevant emission energies are labeled with the chemical element and the diffraction orders.

the refocussing demands on the excitation side are strongly relaxed.

## 3.4 Optimizing the VLS-parameters

Finding the optimum VLS-parameters which determine the variation of the line density along the grating surface means minimizing imaging aberrations for the relevant photon energies and orders. For one energy and order alone, it would be possible to modulate the line density such that the imaging aberrations vanish entirely, leading to a stigmatic image in the dispersive direction. Since in our case four different photon energies in different diffraction orders are of interest (see section 3.1), the optimum VLS-parameters can only be a good compromise. To find the best parameters, rays in the tangential plane emerging from a point source have to be ray-traced through the whole spectrograph, consisting of a spherical mirror, the VLS-grating, and the detector plane. The goal is to minimize the variation of the impinging point on the detector as a function of the meridional angle of the ray emerging from the point source. The algorithm minimizing

this variation was implemented in mathematica®. This software allows to express the impinging point on the detector as an analytical function of the meridional angle and the VLS-parameters as well as the tilt angles of the optical elements and the photon energy of the simulated rays. To optimize a set of parameters for a number of interesting photon energies and orders, the first step is to calculate the boundaries of the meridional angle determined by the dimensions of the mirror and the grating. The range of the meridional angle accepted by the spectrograph is covered by eight equidistant rays. Finally, the distance of the eight impinging points on the detector to the impinging point of the center ray are determined for each relevant photon energy and diffraction order as analytical functions of the parameters to optimize. In our case of four photon energies, this gives a total of 32 functions. The sum of the squared functions is the residual function to minimize. Since this is still expressed in analytical form, the optimization algorithm based on Newton's method can make use of the analytically determined jacobian matrix resulting in a very reliable and quickly converging minimization process even in a high-dimensional parameter space. The optimized parameter sets included up to four VLS-parameters (line density variation up to the quartic term), the detector plane tilt angle, and the distance grating-detector plane. It turned out that tilting and shifting the detector out of the zeroth order focal plane as well as including higher VLS orders than the cubic term does not lead to significantly lower imaging aberrations. Therefore, in the final run three VLS-parameters were optimized (i.e. up to the cubic term) with the detector plane perpendicular to the central incoming ray in the zeroth order focus. The optimization time on a 1.2 GHz Pentium III system was 4 seconds starting with a conventional equally-spaced grating, i.e., with all VLS-parameters set to zero. The derived parameters are listed at the beginning of chapter 2.

# Chapter 4

# Theoretical performance and ray traced images

## 4.1 Energy resolution

In this chapter we will present the theoretical performance of the optimized spectrograph design and prove that it meets the design goal of a resolving power between 850 and 1,000. Furthermore, a good design should show a well-balanced ratio between the three effects limiting the resolving power: source size, pixel size, and imaging aberrations. The broadening of the image in the detector plane due to the source size should be comparable to the imaging aberrations of the fully illuminated optical elements. Masking the mirror can then reduce the latter at the cost of intensity for high resolution measurements. But even without imaging aberrations (i.e., very narrow mirror illumination), the image should still be about three detector pixels wide. As can be seen in Fig. 3.4, in the case of inner orders, the 10 $\mu$m source-size limited resolving power is higher than the pixel resolution. To reduce it to one third of the pixel-limit, a source size of 30 $\mu$m in the dispersive direction is appropriate. Fig. 4.1 shows the pixel-limited (solid line) and the source-limited (dashed line) resolving powers for this case.

## 4.2 Throughput

The final design accepts a solid angle of 11.2x18.5 mrad. The mirror reflectivities and grating efficiencies for the four interesting energies and diffraction orders were calculated with "REFLEC" [3] for a Ni coating with a surface roughness of 10 Å and are listed in the following table.

| emitting element | | sulfur | carbon | nitrogen | oxygen |
|---|---|---|---|---|---|
| emission energy | [eV] | 150 | 280 | 400 | 525 |
| diffraction order | | $1^{st}$ | $2^{nd}$ | $2^{nd}$ | $3^{rd}$ |
| mirror reflectivity | [%] | 68.0 | 66.6 | 65.2 | 59.7 |
| grating efficiency | [%] | 24.7 | 21.6 | 22.4 | 18.5 |
| total transmission | [%] | 17.3 | 14.5 | 14.7 | 11.1 |

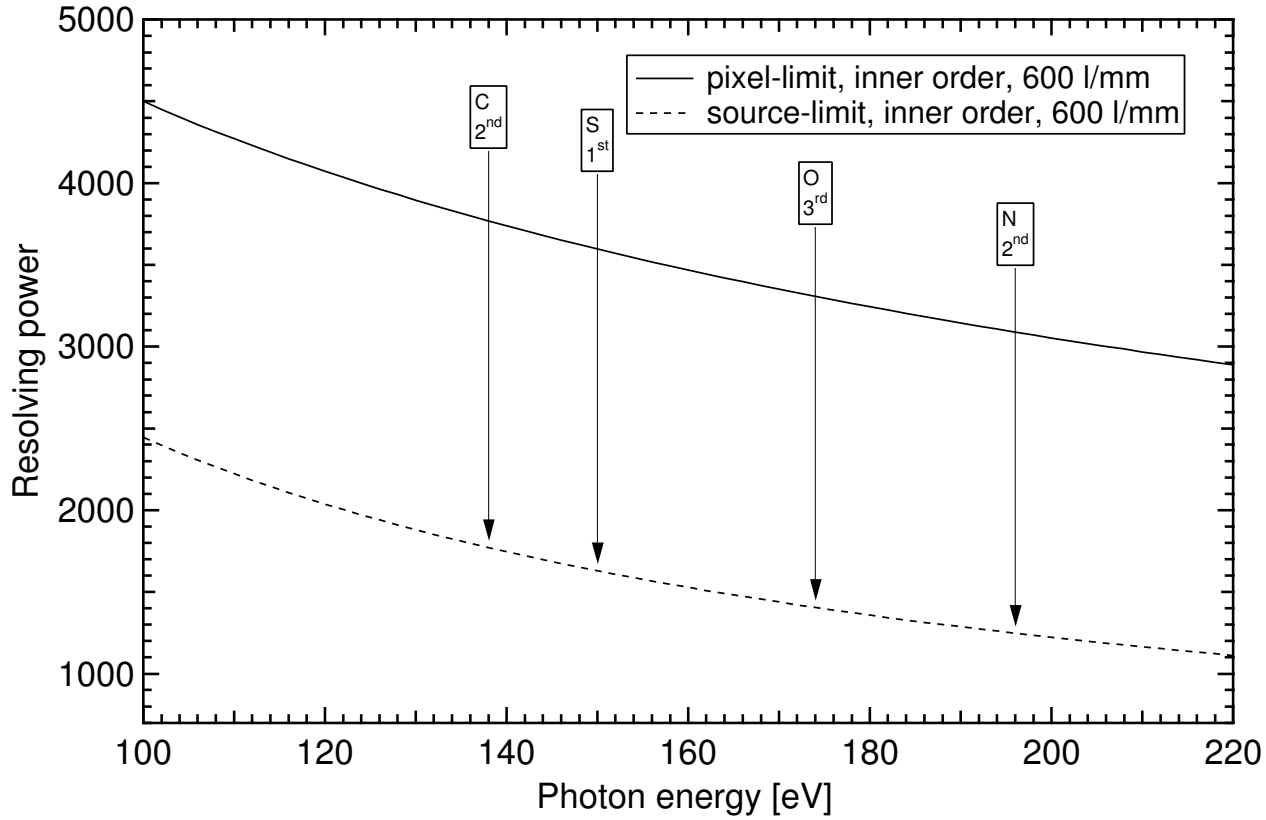


Figure 4.1: The pixel-limited (solid line) and the source-limited resolving power (dashed line) of the final spectrograph design for a source size of 30 $\mu$m in the dispersive direction.

## 4.3 Ray tracing

The following figures 4.2-4.5 show the ray traces produced by "RAY" [4] for the four relevant photon energies and orders. The ray traced photon energy distribution is composed of 3 equidistant discrete energies, where the center energy $h\nu$ is the one mentioned in the caption, and the two adjacent energies are $h\nu \pm \frac{1}{1{,}000} h\nu$. Thus, whenever the three energies can be resolved in the ray traced image, a total resolving power of 1,000 or better was achieved. The divergence of the rectangular source (hard edge, dimensions: 3,000 x 30 $\mu$m$^2$) is 11.2 mrad vertical and 18.5 mrad horizontal, and the detector pixel dimensions are 13.5 x 13.5 $\mu$m$^2$. The center energies and diffraction orders are listed in the figure captions.

The presented ray tracings clearly confirm an energy resolution of 1000 in all cases except for nitrogen, where the three energies are still resolved, but not clearly separated. This is not surprising since the energy resolving power is lowest in this case (see Fig. 4.1). In addition, the imaging aberrations are highest in the N case since this emission line appears furthest away from the optimum energy of 162 eV. Note that the graph bars on the right hand side of the ray traced images show a horizontally integrated spectrum without taking the curvature of the

emission lines on the detector into account. Since the data acquisition software integrates along the experimentally determined curvature, the acquired spectra will be better resolved.

The energy range covered by the detector height of one inch at a center energy of 162 eV is 122 to 228 eV in first order, i.e., all four relevant energies (in their respective orders) fit on the detector simultaneously, without moving any spectrograph components. Thus, potential imprecisions and reproducibility problems caused by mechanical slack are avoided.

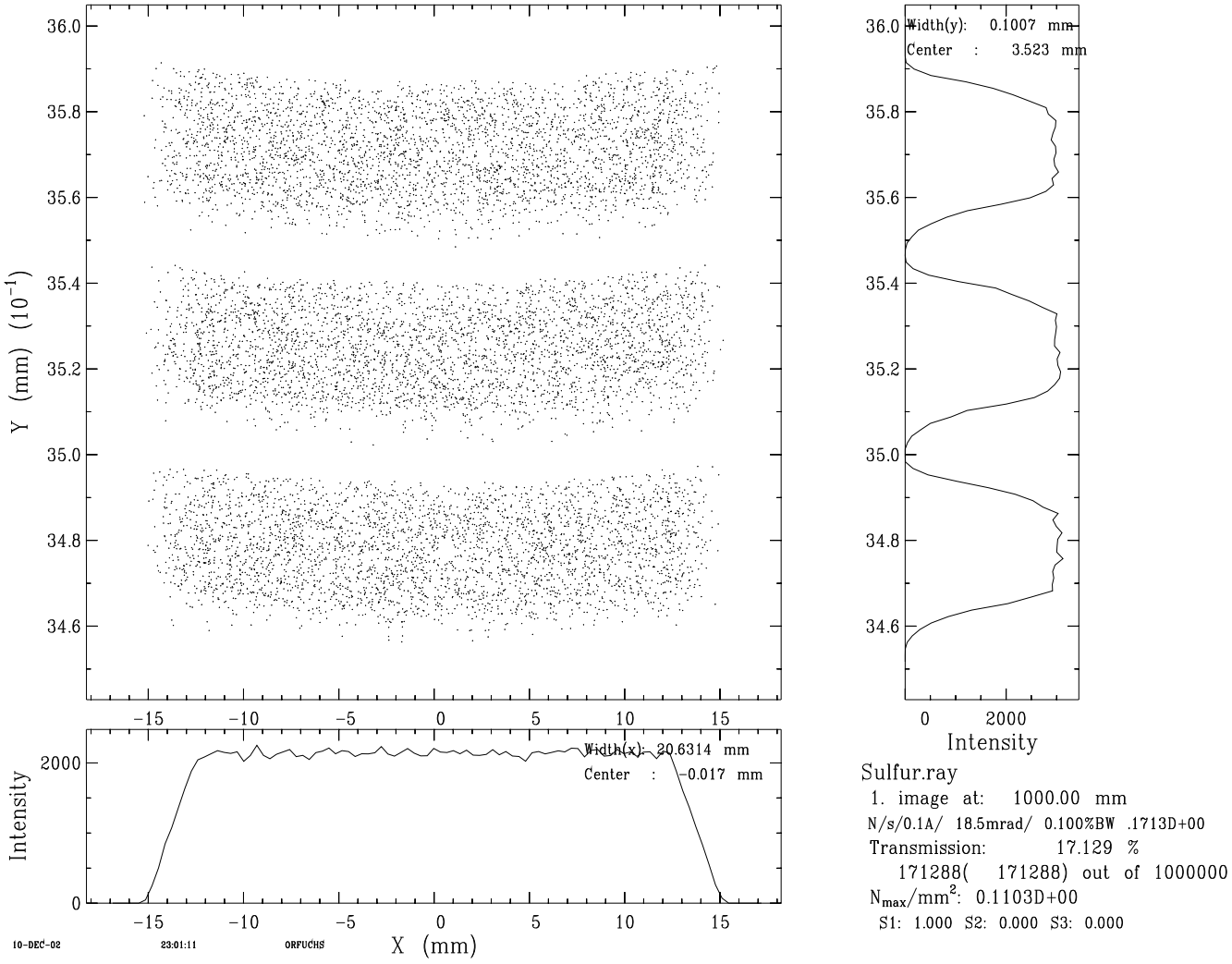


Figure 4.2: Ray tracing at 150 eV (Sulfur $L_{2,3}$ emission), 1st diffraction order.

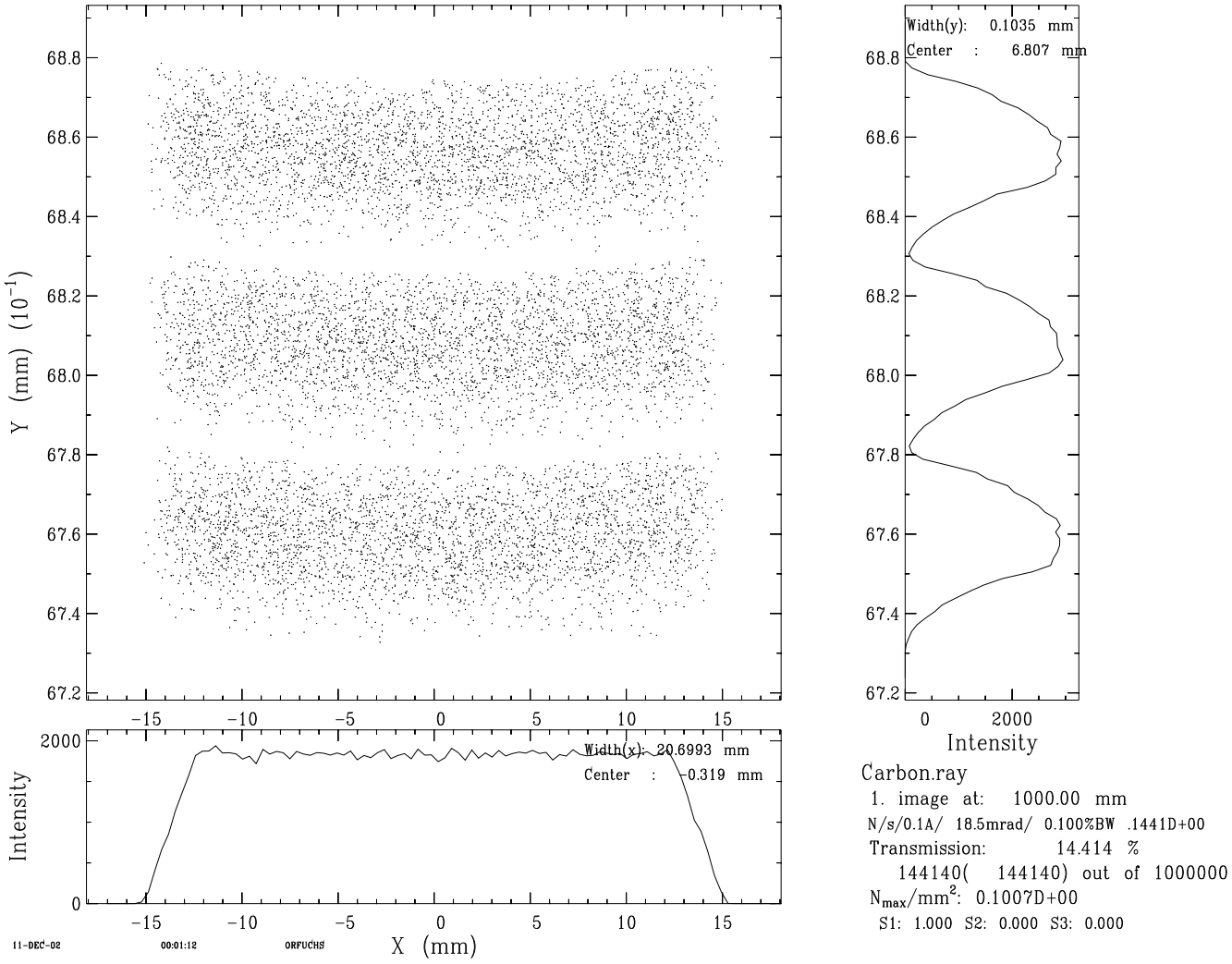


Figure 4.3: Ray tracing at 280 eV (Carbon K emission), 2nd diffraction order.

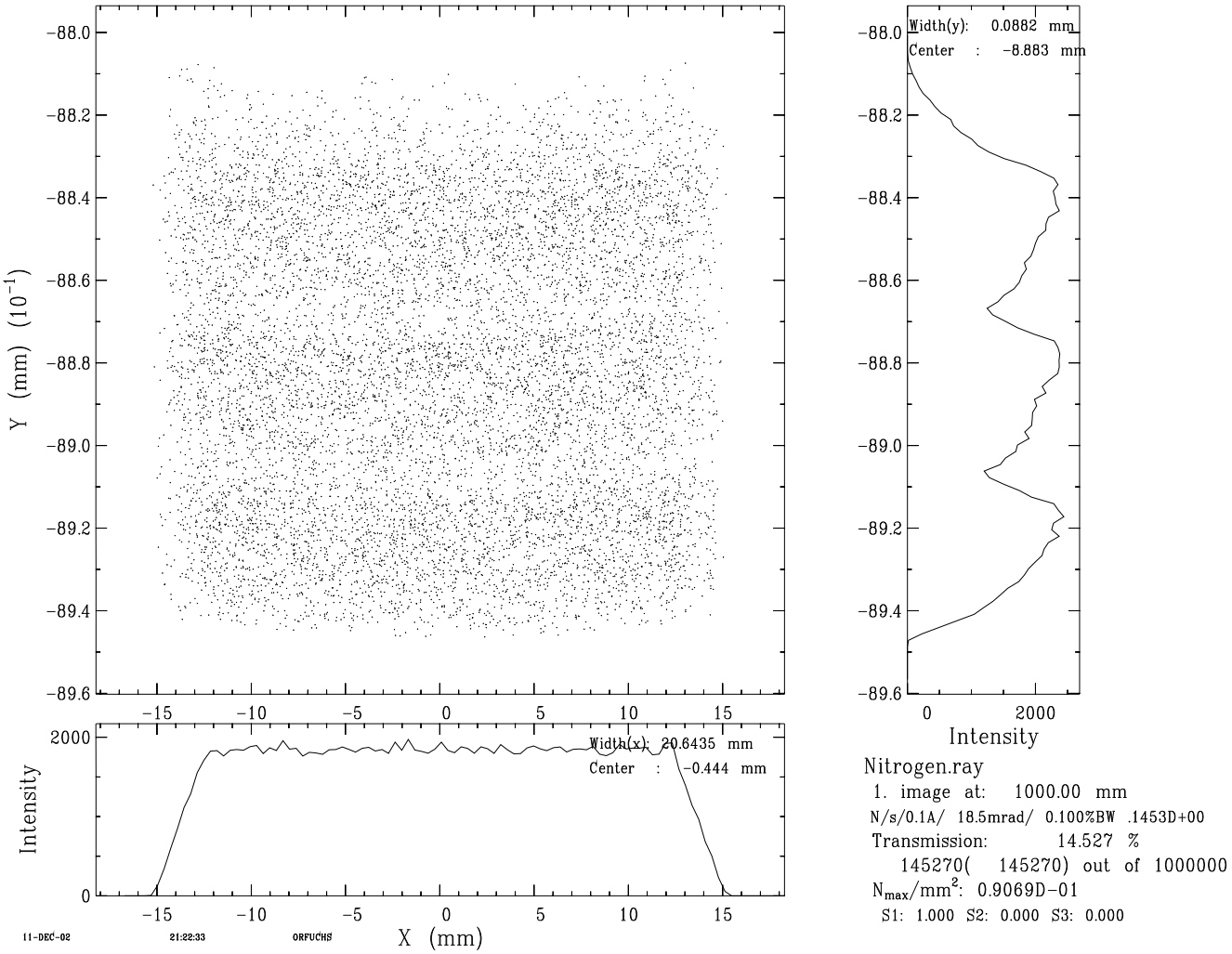


Figure 4.4: Ray tracing at 400 eV (Nitrogen K emission), 2nd diffraction order.

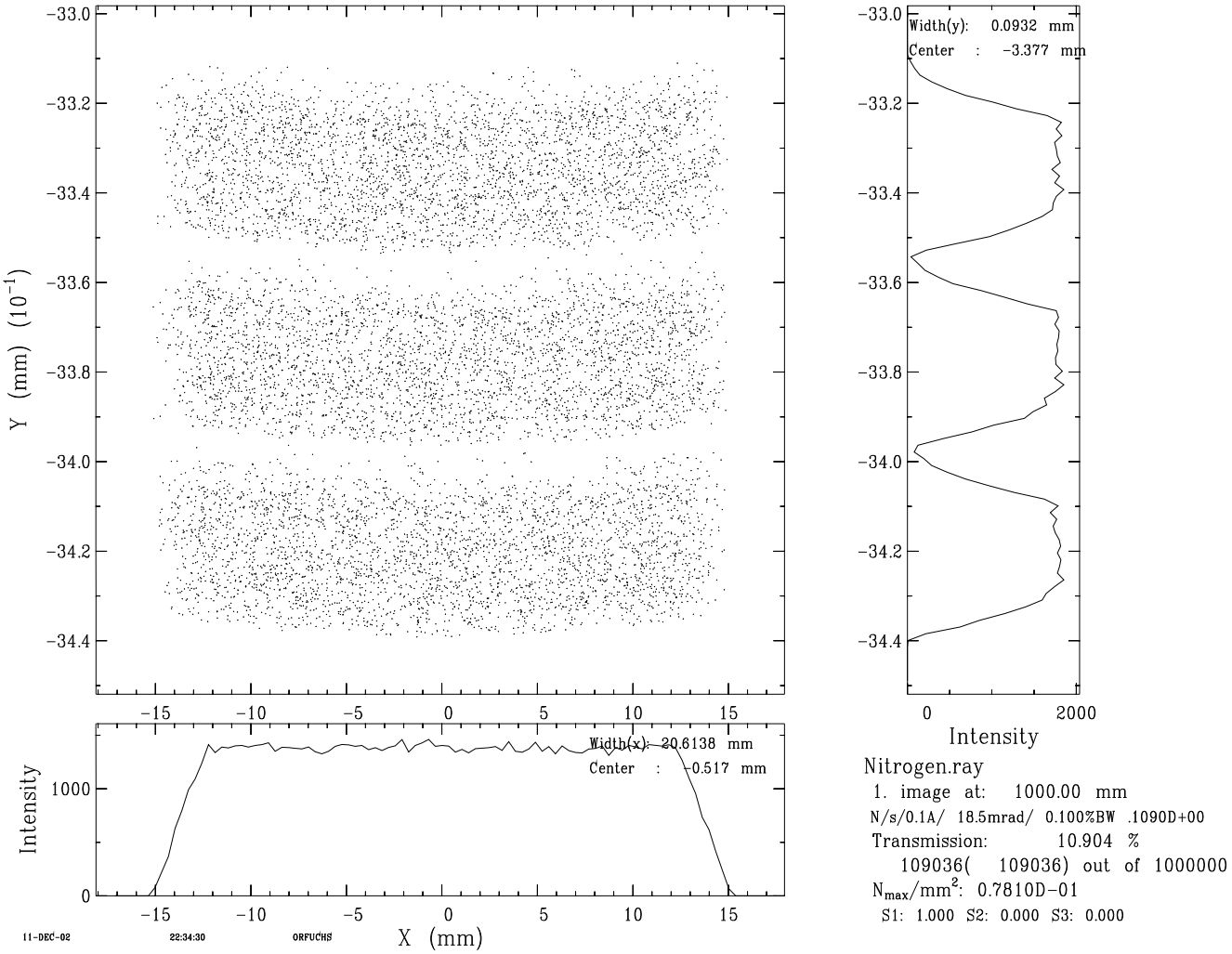


Figure 4.5: Ray tracing at 525 eV (Oxygen K emission), 3$^{rd}$ diffraction order.

# Chapter 5

# Summary

In this report, the design for a soft x-ray spectrograph is presented, which is optimized for the investigation of biologically relevant molecules containing sulfur, carbon, nitrogen, and oxygen atoms. The spectrograph covers a photon energy range from 120 to 550 eV with an energy resolution above 800. Furthermore, it possesses a high throughput, in particular due to a high acceptance angle, which minimizes beam damage effects.

The proposed design consists of a spherical mirror as focussing element, a blazed VLS-grating to introduce the energy dispersion, and a back-illuminated CCD camera as detector. It operates in a slitless mode using the focused illuminated spot on the sample as the source. Each relevant emission energy is recorded in an optimal diffraction order, preserving the high energy resolution and the maximum diffraction efficiency of the blazed grating. The grating works in a constant incidence angle mount with diffraction angles steeper than the incidence angle (so-called inner or positive orders). The desired operation mode requires no mechanical motion such as grating rotation or detector translation, avoiding potential problems due to mechanical inaccuracy and irreproducibility. The accepted solid angle is 11.2 x 18.5 mrad and the calculated overall transmission consisting of the mirror reflectivity and the grating efficiency is in the range of 11 to 17 percent, depending on the photon energy.

# Bibliography


[1] Internal reports of the ALS, **LSBL #622:** Jim Underwood, Zahid Hussain, Wayne R. McKinney, Tony Warwick: *1.5 Meter VLS Emission Spectrometer*

[2] Internal reports of the ALS, **LSBL #623:** Wayne R. McKinney, Tony Warwick: *Analysis and Extension of 1.5 Meter VLS Emission Spectrometer*

[3] Bessy Technische Berichte, **TB 201/96:** F. Schäfers, M. Krumrey: *REFLEC - A Program to Calculate VUV/X-Ray Optical Elements and Synchrotron Radiation Beamlines*

[4] Bessy Technische Berichte, **TB 202/96:** F. Schäfers: *RAY - The BESSY Raytrace Program to Calculate Synchrotron Radiation Beamlines*

[5] M.C. Hutley: *Diffraction Gratings,* **Academic Press, 1982, ISBN 0-12-362980-2**